Compensation Methods for Head Motion Detected During PET Imaging

M. Menke, *Life Senior Member, IEEE,* M. S. Atkins, and K. R. Buckley

***Abstract*— We describe two methods to correct for motion artifacts in head images obtained by positron emission tomography (PET). The methods are based on six–dimensional motion data of the head that have to be acquired simultaneously during scanning. The data are supposed to represent the rotational and translational deviations of the head as a function of time, with respect to the initial head position. The first compensation method is a rebinning procedure by which the lines of response are geometrically transformed according to the current values of the motion data, assuming a cylindrical scanner geometry. An approximation of the rebinning transformations by use of large look-up tables, having the potential of on-line event processing, is presented. The second method comprises post-processing of the reconstructed images by unconstrained or constrained deconvolution of the image or image segments with kernels that are generated from the motion data. We use motion data that were acquired with a volunteer in supine position, immobilized by a thermoplastic head holder, to demonstrate the effects of the compensation methods. Preliminary results obtained with test data indicate that the methods have the potential to improve the resolution of Positron Emission Tomography images in cases where significant head motion has occurred, provided that the head position and orientation can be accurately measured.**

I. Introduction

HEAD movements during brain imaging with Positron Emission Tomography (PET) introduce image blurring. The severity of this type of image degradation increases with increasing spatial resolution of the scanner, with increasing frame acquisition time, and obviously, with increasing head motion [1]. In a cylindrical scanner with 380 mm diameter and a crystal size of approximately 6.5^2 mm^2, for example, a head rotation of less than one degree can change the discrete coordinates of a central line of response. The outcome of a certain deviation of the head position in terms of image degradation does not only depend on the magnitude of the deviation, but also on the fraction of the scan time that this deviation has occurred.

Head movements of more than one degree are particularly common in the case of nonanesthetized patients with movement disorders, e.g., Parkinson's Disease, who are the subjects of a research project at the Hospital of the University of British Columbia, Vancouver, Canada. Even if head-holding devices are used, the head movements severely reduce the diagnostic value of the PET images.

While there are several techniques available to register images reconstructed from *different* PET data frames [2], [3] there is currently no well established technique to correct for the image blurring due to head motion *during* frame acquisition. However, this can be done with simultaneously acquired motion data of the scanned subject.

Daube-Witherspoon *et al.* [4] and Green *et al.* [5] describe a radio frequency based measurement system that uses a patient fixed transducer to measure head motion in the six degrees of freedom. This measurement method is not accurate enough for the purpose of artifact compensation because the magnetic fields generated by the radio frequency emitter are distorted by the scanner. Goldstein *et al.* [6] use stereoscopically operated, position-sensitive detectors to measure the three-dimensional (3-D) positions of three miniature lamps, attached to a head fixed wire frame. These data are then used to calculate the orientation and position of the frame. Alternatively, acoustical and videometric [7], [8] techniques can be used to measure head motion.

This paper describes two different methods to compensate for the image blurring due to head movements during frame acquisition, based on six-dimensional (6-D) motion data that describe the orientation and position of the head. The first method comprises the re-binning of the coordinates of the detector pairs that define a line of response (LOR). The geometrically correct transformations as well as approximations by look-up tables are presented. The second method consists of post-processing of reconstructed images by deconvolution operations, using kernels generated from the motion data.

II. Methods

A. Rebinning of Lines of Response

This section explains how the lines of response that describe the path of the annihilation photons can be geometrically transformed according to the three rotational and three translational coordinates describing the orientation and position of the head as a function of the motion measurement cycle, with respect to the initial patient setup. As far as scanner geometry is concerned, we will restrict ourselves to the geometric specification of a commercial scanner[1] with cylindrical geometry.

In the course of event processing during PET data acquisition, the lines of response are represented in different ways.

Manuscript received November 15, 1994; revised August 28, 1995. This work was supported by the Natural Science and Engineering Research Council of Canada under grant #4020. M. Menke was supported by a Deutsche Forschungsgemeinschaft (Germany) post-doctoral fellowship.

M. Menke and K. R. Buckley are with TRIUMF, Vancouver, B.C., V6T 2A3 Canada.

M. S. Atkins is with the School of Computing Science, Simon Fraser University, Burnaby, B.C., V5A 1S6 Canada.

Publisher Item Identifier S 0018-9499(96)01909-0.

[1] 'ECAT 953 B', Siemens, Knoxville, TN, USA.

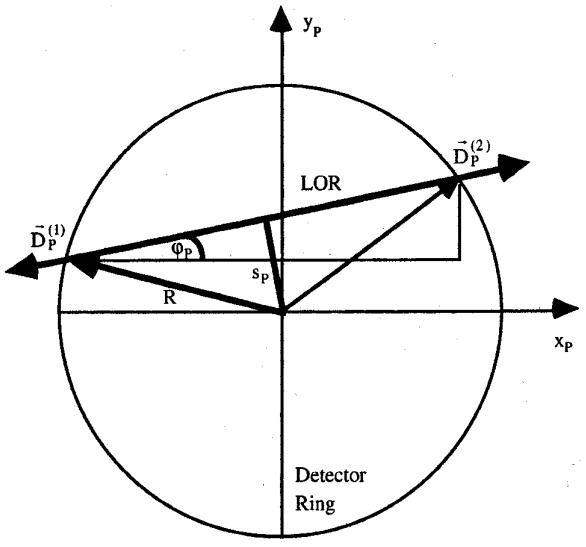

Fig. 1. Conventions for the transformation of lines of response from a sinogram representation to detector positions in the PET coordinate system $\boldsymbol{K}_P$.

The so-called *unformatted* representation of coincident events that is being used in the above mentioned scanner, for example, consists of detector pair coordinates in a hardware oriented notation, involving crystal numbers, bucket[2] pair numbers, and plane numbers. A *formatted* representation comprises the indices of 2-D sinograms (representing the azimuth φ of the LOR, and the distance s of the LOR from the tomograph axis), and the numbers I and J of the detector rings that were involved in the event detection.

However, the relation between the hardware related discrete event representation and the 3-D PET coordinates of two points on the LOR, e.g., the centers of the respective detector crystals, is unambiguous and can be realized by look-up tables. For formatted events, given by the coordinates φ_P, s_P, I_P, J_P, the 3-D coordinates $\vec{D}_P^{(i)}(i = 1, 2)$ of the centers of the corresponding crystal surfaces in the PET coordinate system $\boldsymbol{K}_P$ can be computed as follows (see Fig. 1)

$$\vec{D}_P^{(1)} = \begin{pmatrix} -s_P \cdot \sin\varphi_P - \sqrt{R^2 - s_P^2} \cdot \cos\varphi_P \\ s_P \cdot \cos\varphi_P - \sqrt{R^2 - s_P^2} \cdot \sin\varphi_P \\ \left(I_P - \frac{N_{\text{ring}}+1}{2}\right) \cdot \Delta_{C,a} \end{pmatrix}$$

$$\vec{D}_P^{(2)} = \begin{pmatrix} -s_P \cdot \sin\varphi_P + \sqrt{R^2 - s_P^2} \cdot \cos\varphi_P \\ s_P \cdot \cos\varphi_P + \sqrt{R^2 - s_P^2} \cdot \sin\varphi_P \\ \left(J_P - \frac{N_{\text{ring}}+1}{2}\right) \cdot \Delta_{C,a} \end{pmatrix} \quad (1)$$

with $I_P = 1, \cdots, N_{\text{ring}}$ and $J_P = 1, \cdots, N_{\text{ring}}$. N_{ring} is the (even) number of detector rings, $\Delta_{C,a}$ is the axial crystal separation, and R is the inner radius of the tomograph. The PET coordinate system is assumed to be geometrically centered in the tomograph. In (1), we disregarded the slight deviation of the truly polygonal detector ring from cylindrical geometry.

[2] A "bucket" comprises a number of detector blocks that are simultaneously processed by the coincidence circuitry.

In order to rebin a LOR that has been detected at time τ_k, $(k = 1, \cdots, N_k$; N_k: number of motion measurement cycles acquired during PET scanning), the detector coordinates $\vec{D}_P^{(i)}(\tau_k)$ have to be transformed into the current head coordinate system $\boldsymbol{K}(\tau_k) \equiv \boldsymbol{K}_k$, using the 3 orientation coordinates $\vartheta_x(\tau_k)$, $\vartheta_y(\tau_k)$, $\vartheta_z(\tau_k)$ and the 3 position coordinates $d_x(\tau_k)$, $d_y(\tau_k)$, $d_z(\tau_k)$ of the head in $\boldsymbol{K}_P$, measured at time τ_k

$$\begin{aligned} \vec{D}_k^{(i)} &\equiv \vec{D}_k^{(i)}(\tau_k) = (T_{kP})^{-1} \otimes \vec{D}_P^{(i)}(\tau_k) \\ &= (\hat{R}(\vartheta_z) \cdot \hat{R}(\vartheta_y) \cdot \hat{R}(\vartheta_x))^{-1} \cdot \left(\vec{D}_P^{(i)}(\tau_k) - \begin{pmatrix} d_x \\ d_y \\ d_z \end{pmatrix} \right) \end{aligned} \quad (2)$$

with

$$\hat{R}(\vartheta_x) = \begin{pmatrix} 1 & 0 & 0 \\ 0 & \cos\vartheta_x & -\sin\vartheta_x \\ 0 & \sin\vartheta_x & \cos\vartheta_x \end{pmatrix}$$

$$\hat{R}(\vartheta_y) = \begin{pmatrix} \cos\vartheta_y & 0 & \sin\vartheta_y \\ 0 & 1 & 0 \\ -\sin\vartheta_y & 0 & \cos\vartheta_y \end{pmatrix}$$

$$\hat{R}(\vartheta_z) = \begin{pmatrix} \cos\vartheta_z & -\sin\vartheta_z & 0 \\ \sin\vartheta_z & \cos\vartheta_z & 0 \\ 0 & 0 & 1 \end{pmatrix}. \quad (3)$$

The notation as an inverse coordinate transformation $(\boldsymbol{T}_{kP})^{-1}$ is a consequence of the fact that the coordinates $\vartheta_x(\tau_k)$, $\vartheta_y(\tau_k)$, $\vartheta_z(\tau_k)$, $d_x(\tau_k)$, $d_y(\tau_k)$, and $d_z(\tau_k)$ describe the orientations and positions of head fixed points in the PET coordinate system $\boldsymbol{K}_P$.

In general, the transformed coordinates $\vec{D}_k^{(i)}$ are not on the tomograph's cylindrical detector surface. With

$$\vec{p} = (p_x, p_y, p_z)^T \equiv \vec{D}_k^{(2)} - \vec{D}_k^{(1)}$$

$$\vec{t} = (t_x, t_y, t_z)^T \equiv \vec{D}_k^{(1)} + \frac{\vec{p}}{2} \quad (4)$$

the coordinates $\vec{D}_{k'}^{(i)} \equiv \vec{D}_{k'}^{(i)}(\tau_k)$ of the intersections of the transformed LOR with the tomograph are given by

$$\vec{D}_{k'}^{(i)} = (D_{k',x}^{(i)}, D_{k',y}^{(i)}, D_{k',z}^{(i)})^T = \vec{t} + m_i \cdot \vec{p}. \quad (5)$$

The exponent T indicates the transposition of the vectors. The numbers $m_i (i = 1, 2)$ can be derived from

$$\begin{aligned} R^2 &= (t_x + m_i \cdot p_x)^2 + (t_y + m_i \cdot p_y)^2 \\ &= t_x^2 + t_y^2 + 2m_i \cdot (t_x p_x + t_y p_y) + m_i^2 \cdot (p_x^2 + p_y^2) \end{aligned} \quad (6)$$

resulting in

$$m_i = -\frac{t_x p_x + t_y p_y}{p_x^2 + p_y^2} \mp \sqrt{\left(\frac{t_x p_x + t_y p_y}{p_x^2 + p_y^2}\right)^2 - \frac{t_x^2 + t_y^2 - R^2}{p_x^2 + p_y^2}}. \quad (7)$$

In accordance with Fig. 1, the negative sign of the square root belongs to $i = 1$. Again, we disregarded the polygonal shape of the detector rings.

The new coordinates may represent LOR's that would not have been detected if there had been no head movement, either because the axial coordinates $D^{(i)}_{k',z}$ are outside the tomograph's axial extension, or because the new transaxial coordinates stand for LOR's outside the transaxial field of view of the scanner. These LOR's can therefore be discarded.

Finally, the valid LOR's are transformed to their initial formatted representation by inversion of (1) (see also Fig. 1)

$$\varphi_{k'} = \begin{cases} a\tan\frac{\Delta y}{\Delta x} & \text{for } \Delta x > 0 \\ \pi/2 & \text{for } \Delta x = 0 \\ a\tan\frac{\Delta y}{\Delta x} + \pi & \text{for } \Delta x < 0 \end{cases}$$

$$s_{k'} = \frac{\Delta x \cdot y_1 - \Delta y \cdot x_1}{\Delta x \cdot \cos\varphi_{k'} + \Delta y \cdot \sin\varphi_{k'}}$$

$$I_{k'} = \frac{D^{(1)}_{k',z}}{\Delta_{C,a}} + \frac{N_{\text{ring}} + 1}{2}$$

$$J_{k'} = \frac{D^{(2)}_{k',z}}{\Delta_{C,a}} + \frac{N_{\text{ring}} + 1}{2} \tag{8}$$

with

$$x_i = D^{(i)}_{k',x},\ y_i = D^{(i)}_{k',y}$$

$$\Delta x = x_2 - x_1,\ \Delta y = y_2 - y_1. \tag{9}$$

With appropriate integer round-off operations, the coordinates $\varphi_{k'}$, $s_{k'}$, $I_{k'}$, $J_{k'}$ have the initial formatted representation. Again, we assumed perfectly cylindrical detector rings.

B. Rebinning of Lines of Response by Look-Up Tables

In the previous section, we described the re-binning procedures that transform an arbitrary line of response according to an arbitrary set of 6-D motion data. Considering the relatively low spatial resolution of PET scanners, it seems worthwhile to sacrifice some of the geometric accuracies of the above transformations to less time consuming methods. In this section we will describe how look-up tables (LUT) can be designed to approximate the re-binning procedures of Section II.

The use of look-up tables for LOR re-binning requires a limited number of combinations of LOR coordinates with motion data. The number of combinations is a priori very large, because it is given by the product of the number of valid lines of response in the scanner, and the number of all detectable head positions and orientations. It is therefore necessary to find an appropriate subset of all combinations.

Given a sinogram representation of the LOR space, consisting of $N_\varphi = 96$ azimuth bins, $N_s = 128$ radial bins, and $N_\psi = 16 \cdot 16 = 256$ polar bins (like in 3-D acquisition mode with retracted septa), the number N_{LOR} of valid LOR's is $N_{\text{LOR}} = N_\varphi \cdot N_s \cdot N_\psi = 3,145,728$. Assuming that, for the purpose of motion artifact compensation, $N_\varphi = N_s = 8$ evenly distributed azimuth and radial bins, and $N_\psi = 2 \cdot 2$ axial bins are sufficient to account for the LOR diversity, the number of LOR's could be reduced to $N_{\text{LOR}} = 8 \cdot 8 \cdot 4 = 256$.

TABLE I
SAMPLING SCHEME FOR A 6-D MOTION DATA SPACE

	Bin Size	Lower Limit	Upper Limit	Number of Bins
ϑ_x [deg]	$2 \approx 2 \cdot \text{ATN}(\Delta_{C,a}/2R)$	-10	20	16
ϑ_y [deg]	$2 \approx 2 \cdot \text{ATN}(\Delta_{C,a}/2R)$	-10	10	11
ϑ_z [deg]	$2 \approx 2 \cdot \text{ATN}(\Delta_{C,t}/2R)$	-16	16	17
d_x [mm]	$\Delta_{C,t}$	-18.75	18.75	7
d_y [mm]	$\Delta_{C,t}$	-12.5	12.5	5
d_z [mm]	$\Delta_{C,a}$	-13.5	27	7

R = 190.7 mm: inner radius of the tomograph
$\Delta_{C,a}$ = 6.75 mm: axial crystal separation
$\Delta_{C,t}$ = 6.25 mm: transaxial crystal separation
ATN: "Arcus Tangens"

Table I shows a possible discrete representation of the 6-D motion data space. The bin sizes of the coordinates are given as functions of the crystal dimensions and the radius of the ECAT 953 B. The upper and lower limits of the coordinates reflect the assumption of limited head motion, e.g. due to a constraining device like a head mask.

The product N_M of the number of bins given in Table I is $N_M = 733\,040$. In this case, the number N_{LUT} of LUT entries is given by $N_{\text{LUT}} = N_{\text{LOR}} \cdot N_M = 256 \cdot 733,040 = 187\,658\,240$. With an element size of 4 bytes, the specified LUT would require approximately 750 Mbytes of memory. These memory requirements can nowadays be met by VME boards.

Using a reduced number of LOR's, the re-binning procedure could be realized by two table look-ups. The first LUT (for the current LOR) would contain the indices of the respective representative LOR, whereas the second LUT would contain the actual index increment that had to be added to the index of the current LOR, depending on the current values of the discrete motion data.

C. Deconvolution of PET Images

In contrast to processing the PET data prior to image reconstruction, the final image data sets can be post-processed by deconvolution type operations to compensate for the motion artifacts. For this purpose, normalized frequency distributions $f_{\vec{O}}$ of the deviations of all positions

$$\vec{O}_P(\tau_k) = (O_{P,x}(\tau_k),\ O_{P,y}(\tau_k),\ O_{P,z}(\tau_k))^T = T_{kP} \otimes \vec{O} \tag{10}$$

from a given initial position $\vec{O}_P(\tau_0) \equiv \vec{O} = (O_x,\ O_y,\ O_z)^T$,

are calculated by use of the 6-D motion data

$$f_{\vec{O}}\begin{pmatrix}\text{int}\,(O_{p,x}(\tau_k)-O_x),\\ \text{int}\,(O_{p,y}(\tau_k)-O_y),\\ \text{int}\,(O_{p,z}(\tau_k)-O_z)\end{pmatrix}=\sum_{\substack{k=1,\cdots,N_k \text{ with}\\ T_{kP}\otimes\vec{O}=\vec{O}_P(\tau_k)}}\frac{\tau_k-\tau_{k-1}}{\tau_{N_k}-\tau_0}. \tag{11}$$

The symbol "int" indicates the integer round-off operation that is necessary to bin the measured deviations to a 3-D grid that is compatible with the discrete image data set. The sum extends over all cycles k for which the transformed position $\vec{O}_P(k)=\boldsymbol{T}_{kP}\otimes\vec{O}$ is on the voxel (volume element) that is specified in the argument of $f_{\vec{O}}$. In other words: the value of $f_{\vec{O}}$ at a certain position is given by the fraction of the measurement time that this position was occupied during measurement.

In (11) we assumed that the activity of the isotope did not change during measurement. The decreasing severity of head movements in the course of scanning due to the decay of the isotope can be accounted for by use of the following equation

$$\begin{aligned}f_{\vec{O}}&\begin{pmatrix}\text{int}\,(O_{p,x}(\tau_k)-O_x),\\ \text{int}\,(O_{p,y}(\tau_k)-O_y),\\ \text{int}\,(O_{p,z}(\tau_k)-O_z)\end{pmatrix}\\ &=\sum_{\substack{k=1,\cdots,N_k \text{ with}\\ T_{kP}\otimes\vec{O}=\vec{O}_P(\tau_k)}}\frac{\int_{\tau_{k-1}}^{\tau_k}\exp\left(-\frac{\tau}{T_{1/2}/\ln 2}\right)d\tau}{\int_{\tau_0}^{\tau_{N_k}}\exp\left(-\frac{\tau}{T_{1/2}/\ln 2}\right)d\tau}\\ &=\sum_{\substack{k=1,\cdots,N_k \text{ with}\\ T_{kP}\otimes\vec{O}=\vec{O}_P(\tau_k)}}\frac{\exp\left(-\frac{\tau_{k-1}}{T_{1/2}/\ln 2}\right)-\exp\left(-\frac{\tau_k}{T_{1/2}/\ln 2}\right)}{\exp\left(-\frac{\tau_0}{T_{1/2}/\ln 2}\right)-\exp\left(-\frac{\tau_{N_k}}{T_{1/2}/\ln 2}\right)}.\end{aligned} \tag{12}$$

$T_{1/2}$ is the half life of the isotope used for imaging.

If the width of the functions $f_{\vec{O}}$, evaluated anywhere within a region of interest (ROI) in the field of view of the scanner, is comparable to the voxel size of the image cube, it makes sense to use the functions $f_{\vec{O}}$ for unconstrained or constrained deconvolutions of the image or of image segments. (The width of the functions $f_{\vec{O}}$ in either dimension may be specified as, for example, four standard deviations.)

Assuming relatively noiseless images and negligible head rotations, the 3-D image data set $I(i, j, k)$ can be processed by a global deconvolution with a function $f_{\vec{O}(0)}(i, j, k)$, evaluated at e.g., the center $\vec{O}^{(0)}$ of the PET coordinate system $\boldsymbol{K}_P$. In this context, the function $f_{\vec{O}(0)}(i, j, k)$ is regarded as an approximation of a shift invariant "motion-point spread function." In the frequency domain, the deconvolution operation can be described as a multiplication of the Fourier transform $FI(\omega_i, \omega_j, \omega_k)$ of the image $I(i, j, k)$ with the "inverse filter"

$$G(\omega_i, \omega_j, \omega_k)=\frac{1}{Ff_{\vec{O}(0)}(\omega_i, \omega_j, \omega_k)} \tag{13}$$

with $Ff_{\vec{O}(0)}(\omega_i, \omega_j, \omega_k)$ being the Fourier transform of $f_{\vec{O}(0)}(i, j, k)$. The deblurred image $ID(i, j, k)$ then has the form

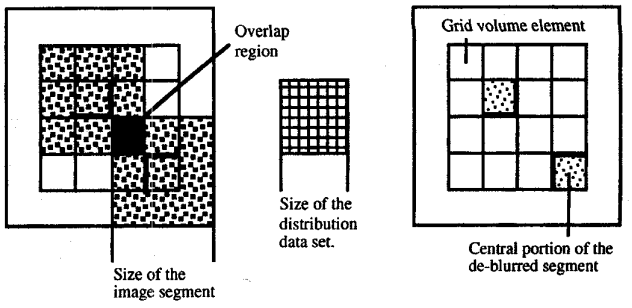

Fig. 2. Two-dimensional illustration of the segmentation of a blurred image cube for local filter operations. Only the central portions of the filtered segments are used to compose the deblurred image cube. Here, the size of the margin around the blurred input image segment has been chosen to account for the full size of the distribution data set, which is much larger than the actual width of the frequency distribution.

$$ID(i, j, k)=F^{-1}(FI(\omega_i, \omega_j, \omega_k)\cdot G(\omega_i, \omega_j, \omega_k)). \tag{14}$$

F^{-1} denotes the inverse Fourier transformation.

In cases of significant rotational contributions to the head movements, the assumption of shift invariance of the functions $f_{\vec{O}}$ is not justified. However, the image data set can be processed *locally* by unconstrained or constrained deconvolutions of image segments $I^{(g)}(i, j, k)$, using frequency distributions $f_{\vec{O}^{(g)}}(i, j, k)$ evaluated at the centers $\vec{O}^{(g)}$ of the corresponding image segments. In particular, the functions $f_{\vec{O}^{(g)}}(i, j, k)$ may be generated for a set of points $\vec{O}^{(g)}$ on a regularly spaced grid ('g') over the image cube, with the grid size chosen fine enough to account for the amount of shift *variance* of the functions, but large as compared to the widths of these functions. The input image segments $I^{(g)}(i, j, k)$ accordingly should have the size of a grid volume element, plus a margin of at least the width of the frequency distributions (see Fig. 2). The latter accounts for the fact that relevant image information for the grid volume element under consideration has been distributed into neighboring volume elements according to the function $f_{\vec{O}^{(g)}}(i, j, k)$, and thus has to be considered for the restoration process.

The fact that neighboring volume elements also contain information that is irrelevant for the volume element under consideration leads to noise amplification. For this reason, the inverse filter is generally inappropriate for the local deblurring operations (see the bar artifacts in Fig. 7, row 4). An alternative filter function that does allow for local image restoration is the following:

$$G(\omega_i, \omega_j, \omega_k)=\frac{[Ff_{\vec{O}^{(g)}}(\omega_i, \omega_j, \omega_k)]^*}{|Ff_{\vec{O}^{(g)}}(\omega_i, \omega_j, \omega_k)|^2+\gamma}. \tag{15}$$

The symbol "*" denotes the complex conjugate of the function. γ is a constant that has to be tuned to suppress the undesired amplification of image frequencies that are not present in $Ff_{\vec{O}^{(g)}}(\omega_i, \omega_j, \omega_k)$. This filter is closely related to the Wiener filter, where γ is replaced by the ratio of the power spectra of noise and signal [9].

III. Results

The results presented below are preliminary:

1) because there was no equipment available to record patient motion during PET imaging at the PET site of the University of British Columbia (UBC), and
2) because the scanner at the UBC PET site did neither have list mode acquisition option for an a posteriori re-binning of the PET raw data, nor did it have the hardware capabilities to perform on-line re-binning.

The first argument has the consequence that the motion data that we used were not correlated to any PET data. This, and the missing re-binning capabilities of the PET scanner imply that the two compensation methods could not directly be compared to each other.

Subsection A describes how the motion data were acquired, subsection B compares results of geometrically exact rebinning transformations with those from look-up table approximations, using the motion data of subsection A, and subsection C compares the results of *global* and multiple *local* deconvolution operations applied to an artificially blurred PET image, again using the motion data of subsection A.

A. Motion Measurements

We have performed videometric motion measurements with a volunteer in supine position, immobilized by a thermoplastic head holder that is commonly used for PET imaging. The measurements were performed in a dental laboratory of the University of British Columbia.

We used a commercial motion analysis system,[3] based on two infra-red sensitive CCD video cameras. The measurement accuracy for the determination of the 3-D position of an optical target was approximately 0.2 mm within the calibrated working volume. The optical targets consisted of three circular pieces of infra-red reflective tape that were affixed to a lightweight landmark device. The landmark device itself was rigidly attached to the teeth of the subject's upper jaw, using dental cement and a maxillary splint made of acrylic resin.

The acquisition rate for the videometric measurements was 50 Hz. We acquired five data sets of 30 seconds duration each, over a period of approximately 30 minutes. For processing with the compensation methods, the data sets were combined to a single file, representing a measurement duration of 2.5 minutes, with slight discontinuities every 30 seconds.

The motion data acquired consisted of the 3D positions of the three reflective markers, given in the reference coordinate system $\boldsymbol{K}_V$ of the videometric system. The system $\boldsymbol{K}_V$ was defined by the position and orientation of a device that was used for the calibration of the camera system. Because the placement of the calibration device was unrelated to any PET scanner, the coordinate transformation of the motion data into the PET coordinate system $\boldsymbol{K}_P$ was unknown. However, we estimated the parameters for the transformation into the ECAT system by use of fiducial markers on the head holder. The camera coordinates of the optical markers could thus be transformed into a coordinate system that was similar to the PET coordinate system $\boldsymbol{K}_P$.

[3] "MacReflex" System, Qualisys, Sweden.

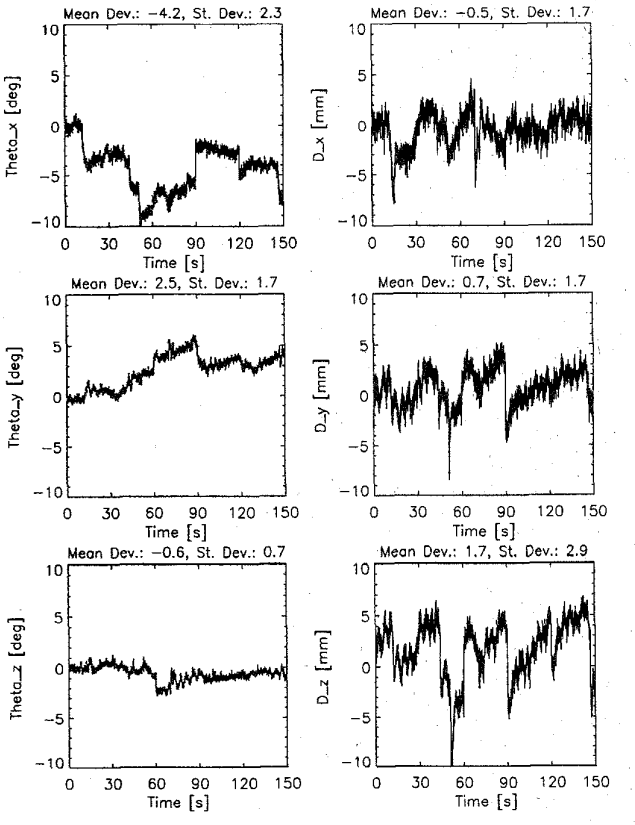

Fig. 3. 6-D representation of the motion data that were used to demonstrate the effects of the compensation methods. We acquired 7500 motion data sets at 50 Hz acquisition rate, resulting in a measurement duration of 150 seconds.

The marker coordinates were post-processed to determine the six motion coordinates of the marker-head-system with respect to the initial setup in $\boldsymbol{K}_P$, using an iterative fitting procedure based on the Levenberg-Marquardt Chi-Square minimization algorithm [10].

Because the volunteer was a healthy 27-year-old male, the movements we measured were to small to demonstrate the effects of the different compensation methods. For this reason, we multiplied each of the six motion coordinates with a factor of 10 before processing them. The modified 6-D motion data are presented in Fig. 3. Note the relatively larger rotational deviations around the x-axis, indicating insufficient suppression of nodding rotations by the head mask.

B. Rebinning of Event Lines

The geometric re-binning transformations described in (2), (5), and (8), including a test of the validity of the transformed LOR, take approximately 50 microseconds CPU time on a "Sun Sparc 2" computer, using FORTRAN code. The respective time for a table look-up is in the order of a few microseconds. Disregarding the errors that are related to the discretization and limitation of the LOR space and the motion data space, the use of look-up tables on faster computers has thus the potential for on-line re-binning of events that are acquired at MHz rate.

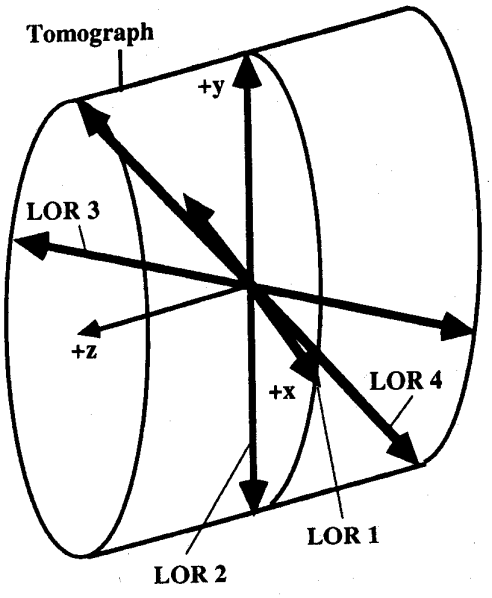

Fig. 4. Choice of test LOR's for the re-binning procedures. LOR 1 and 3 are in the x-z plane, LOR 2, and 4 are in the y-z plane.

Using the motion data shown in Fig. 3, we have applied the rebinning procedures to four test LOR's (Fig. 4), given in a sinogram representation, and evaluated the deviations of the transformed discrete LOR coordinates from their initial values. The results for the geometrically correct transformations and the approximations by look-up tables, using the motion data discretization presented in Table I, are illustrated in Fig. 5 and Table II.

The data presented for the four test LOR's do not show major variations with the two different re-binning procedures. This indicates that the look-up table concept might be an appropriate approximation of the geometrically exact transformations.

C. Local Deconvolution of PET Images

The effect of *local* filter operations on an artificially blurred PET image was studied as follows: we first blurred an image data set by local convolutions of image segments with normalized frequency distributions that had been evaluated at the centers of each segment, using the motion data presented in Fig. 3. We then applied different de-blurring operations on *larger* segments to simulate the effect of a finite segmentation grid that would be used to de-blur an actually motion-blurred patient image.

The PET image cube that we used was reconstructed from a 30 minute raclopride scan (Carbon 11) that had been acquired in 3-D mode with retracted septa. For image processing, we extracted a central cube of $64 \cdot 64 \cdot 16$ voxels from the original image ($128 \cdot 128 \cdot 31$) voxels, see Fig. 6 and Fig. 7, row 1).

We then decomposed the central cube into $8 \cdot 8 \cdot 4$ segments of $8 \cdot 8 \cdot 4$ voxels in size, and convolved each segment with the corresponding centered normalized frequency distribution, evaluated on a $16 \cdot 16 \cdot 16$ voxel grid. The results of the convolutions were rearranged into a new image cube of

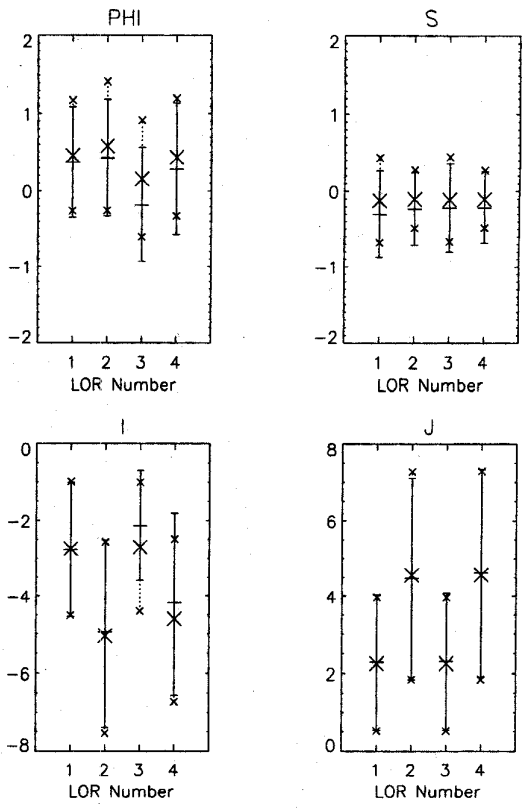

Fig. 5. Mean and standard deviations of the *discrete* LOR coordinates φ, s, I, and J, from their initial values (see Fig. 4), calculated with the geometrically exact transformations (horizontal bars and vertical solid lines) and with table look-up (crosses and dotted lines), using the motion data discretization presented in Table I. The vertical lines extend over a range of two standard deviations, centered at the mean deviation.

TABLE II
NUMBER OF EVENTS THAT FELL OUT OF THE VALID RANGE, GIVEN BY THE AXIAL EXTENSION OF THE TOMOGRAPH AND THE TRANSAXIAL FIELD OF VIEW OF THE SCANNER, FOR THE GEOMETRICALLY EXACT TRANSFORMATIONS AND FOR TABLE LOOK-UP. THE TOTAL NUMBER OF REBINNING TRANSFORMATIONS WAS 7500

	LOR 1	LOR 2	LOR 3	LOR 4
Exact	0	1411	6681	7036
Table look-up	0	1738	6639	7100

$(64+16) \cdot (64+16) \cdot (16+16)$ voxels. The images shown in row 2 of Fig. 7 show the effect of the simulated (additional) head motion, explicitly taking into account the effect of shift *variant* contributions by local blurring operations with the respective kernels.

The first de-blurring operation we applied was a deconvolution of the central cube, treated as one segment, with the corresponding centered kernel. The resultant image (Fig. 7, row 3) was similar to the original image, except for some restoration errors towards the edges of the image cube and an unsatisfactory reconstruction of the voxel values in the basal ganglia. For a quantification of the restoration quality see the caption of Fig. 7.

Row 4 in Fig. 7 shows the result of 32 local de-blurring operations, applied to 32 equally sized segments of the cen-

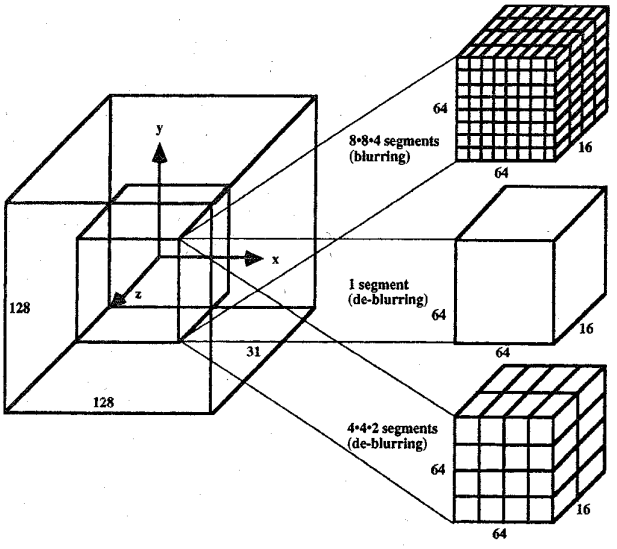

Fig. 6. Segmentation of the raclopride image cube for local blurring and de-blurring operations. The numbers given are the dimensions of the data sets in voxels (not to scale).

tral cube (see Fig. 6), using the inverse filter. Due to an overlap of the different input image segments, bar artifacts appear and deteriorate the quality of the reconstructed images significantly.

The bar artifacts can be avoided using the modified Wiener filter with an appropriate value for the parameter γ. The images presented in row 5 of Fig. 7 were obtained with

$$\gamma = 0.01 \cdot \max\left(|Ff_{\vec{O}(g)}(\omega_i, \omega_j, \omega_k)|^2\right). \qquad (16)$$

These images are the best approximation of the original data set in terms of the standard deviation of the voxel values.

The data presented in Fig. 7 show that, in cases of shift variant "motion kernels," the application of *local* filter operations can have an advantage over a simple deconvolution of the whole image cube.

IV. Discussion

A. Motion Measurements

The motion data that we used to simulate artifact compensation were artificial because of the following: first, the parameters for the transformation of the motion data into the PET coordinate system had to be estimated because the videometric measurement setup was not directly related to a PET scanner, second, the voluntary subject did not have any movement disorders, and third, the measured 6-D motion data were multiplied by a factor of 10, to simulate the larger movements expected with patients with movement disorders. The fact that the motion data were not correlated with the PET data that we investigated in the previous section (test LOR's, patient images) implies that the results we presented (LOR statistics, de-blurred images) do not account for motion measurement errors that would otherwise negatively affect the accuracy of the compensation methods.

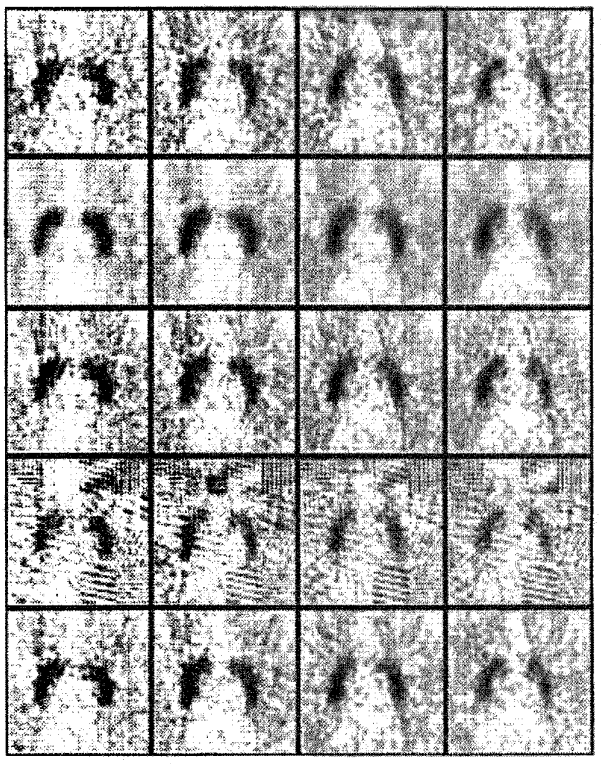

Row no.	Operation	Standard Dev. [%]
1	None (original image data set)	0
2	Blurring: convolution with 8•8•4 kernels	6.65
3	De-blurring: Inverse filter, 1 kernel	5.39
4	De-blurring: Inverse filter, 4•4•2 kernels	11.03
5	De-blurring: Modified Wiener filter, 4•4•2 kernels	3.59

Fig. 7. Results of de-blurring operations applied to an artificially blurred 3-D PET image of a 30-minute raclopride scan (C11). The rows (numbered top to bottom) show four central planes of a $64 \cdot 64 \cdot 16$ voxel cube that had been extracted from the original image (see Fig. 6). The active areas (dark) show the basal ganglia of the patient. The table below lists the standard deviations of the voxel values in the manipulated images from the voxel values in the original image data set. The smallest standard deviation is obtained with the modified Wiener filter with the γ-value given in (16).

We have recently installed a videometric measurement system at the PET department of the Hospital of the University of British Columbia (UBC), Vancouver, Canada. With this system, the relation between the videometric and the PET coordinate systems is established by a calibration device that can be aligned with the positioning lasers of the PET scanner. We will start a trial with voluntary patients with movement disorders to acquire videometric motion data simultaneously with PET imaging. This will allow us to investigate the effect of motion measurement errors on the outcome of the deconvolution methods.

Apart from using the motion data for compensation for movements that occurred *during* frame acquisition, we will also investigate the potential for an application to inter-frame

alignment of subsequent emission frames or transmission and emission frames.

B. Compensation Methods

Compensation for head movements can in principle also be done by subject repositioning [8]. Without sophisticated mechanics to compensate for head rotations, however, these methods lack adequate compensation for rotational deviations. The two methods that we presented use the motion data to correct the PET data in all six dimensions.

If the PET scanner allows for list mode data acquisition, the geometrically exact re-binning transformations, that are too slow for on-line event processing in scanners with acquisition rates of 1 MHz or more, may be used to post-process the event coordinates, prior to image reconstruction. Without list mode option, approximations by look-up tables may be used for this purpose, at the cost of additional memory boards of Gigabyte size. Further research will have to deal with the best trade-off between memory requirements and accuracy for a given scanner geometry and the estimated range of head movements.

The geometric re-binning transformations that we presented are *not* compatible with the detector normalization methods that are commonly applied to PET sinograms to correct for intrinsic and geometric differences in detector efficiencies within the scanner, because re-binned lines of response would be incorrectly weighted with the normalization factor that accounts for the efficiency of the detectors belonging to the *transformed* line of response, and not with the factor for the crystal that actually detected the event. The corresponding error depends on the variation of the respective normalization matrix over the sinogram space. An investigation of the magnitude of this error will be subject of further research. However, the geometric re-binning procedures are compatible with 3-D methods of PET data acquisition because they are not restricted to planar lines of response.

Image de-blurring by local filter operations with the modified Wiener filter requires tuning of the constant γ. The trade-off is between the suppression of bar artifacts that are related to the overlap of the blurred input image segments, and the suppression of additional image blurring that increases with an increasing value of γ. If the region of interest in the image is localized within a small volume, the tuning of γ can be avoided, or at least simplified, by use of a global filter operation of the whole image cube, with the filter function evaluated at the center of the specified region.

We believe that the application of these methods will allow us to obtain images with higher resolution than is currently available for scans where significant head motion has occurred.

ACKNOWLEDGMENT

The authors would like to thank Dr. A. Hannam, Faculty of Dentistry, University of British Columbia (UBC), Vancouver, Canada, and his colleagues for their help and their permission to perform measurements with their videometric equipment. They also acknowledge valuable discussions with Dr. V. Sossi and S. Morrison from the UBC PET research group.

REFERENCES

[1] E. J. Hoffman and M. E. Phelps, "Positron emission tomography: Principles and quantitation," in *Positron Emission Tomography and Autoradiography. Principles and Applications for the Brain and Heart*, M. E. Phelps, J. C. Mazziotta, and H. R. Schelbert, Eds. New York: Raven, 1986, pp. 237–286.

[2] R. P. Woods, S. R. Cherry, and J. C. Mazziotta, "Rapid automated algorithm for aligning and reslicing PET images," *J. Comp. Ass. Tom.*, vol. 16, pp. 620–633, 1992.

[3] Q.-S. Chen, "Image registration and its application in medical imaging," Vrije Universiteit Brussel, Ph.D. dissertation, 1993.

[4] M. E. Daube-Witherspoon, Y. C. Yan, M. V. Green, R. E. Carson, K. M. Kempner, and P. Herscovitch, "Correction for motion distortion in PET by dynamic monitoring of patient position," *J. Nuc. Med.*, vol. 31, pp. 816, 1990. (Abstract.)

[5] M. V. Green, J. Seidel, S. D. Stein, T. E. Tedder, K. M. Kempner, C. Kertzman, and T. A. Zeffiro, "Head movement in normal subjects during simulated PET brain imaging with and without head restraint," *J. Nuc. Med.*, vol. 35, pp. 1538–1546, 1994.

[6] S. R. Goldstein, M. E. Daube-Witherspoon, and M. V. Green, "A device for continuous measurement of head position during PET brain imaging," *J. Nuc. Med.*, vol. 35, p. 40P, 1994. (Abstract).

[7] M. Menke, F. Hirschfeld, T. Mack, O. Pastyr, V. Sturm, and W. Schlegel, "Photogrammetric accuracy measurements of head holder systems used for fractionated radiotherapy," *Int. J. Radiat. Oncol. Biol. Phys.*, vol. 29, pp. 1147–1155, 1994.

[8] Y. Picard, C. J. Thompson, "Digitized Video Subject Positioning and Surveillance System for PET," in *Proc. IEEE 1994 Medical Imaging Conf.*, Norfolk, VA, 1994.

[9] S. Webb, A. P. Long, R. J. Ott, M. O. Leach, and M. A. Flower, "Constrained deconvolution of SPECT liver tomograms by direct digital image restoration," *Med. Phys.*, vol. 12, pp. 53–58, 1985.

[10] W. H. Press, B. P. Flannery, S. A. Teukolsky, and W. T. Vetterling, *Numerical Recipes. The Art of Scientific Computing.* Cambridge University Press, 1987.